Journal of Aeronautics, Astronautics and Aviation, Vol. 52, No. 4, pp. 429 – 442 (2020)
DOI: 10.6125/JoAAA.202012_52(4).07

Ensuring High Navigation Integrity for Urban Air Mobility Using Tightly Coupled GNSS/INS System *

Shizhuang Wang, Xingqun Zhan **, Yawei Zhai, Cheng Chi, and Xiyu Liu

School of Aeronautics and Astronautics, Shanghai Jiao Tong University
No.800, Dongchuan Rd., Minhang District, Shanghai 200240, China.

ABSTRACT

The industry is pursuing Urban Air Mobility (UAM) to offer short-range, point-to-point air transportation services in metropolitan areas. This concept has the potential to mitigate ground-based congestion and improve transportation efficiency. To ensure the safety of UAM operations, the airborne navigation system must provide accurate and reliable navigation information. However, the design of such navigation systems remains not fully addressed in prior studies. Accordingly, this paper firstly presents a high-accuracy navigation system that employs Global Navigation Satellite Systems (GNSS)/ Inertial Navigation System (INS) tight integration and exploits differential GNSS corrections. Then, to protect against the potential measurement faults caused by complex signal reflections in urban environments, an Aircraft Autonomous Integrity Monitoring (AAIM) framework is developed by applying multiple hypotheses solution separation to the Kalman filter-based integration architecture. This framework offers two capabilities of essential importance to ensuring safe UAM operations: real-time fault detection and rigorous navigation integrity quantification. The proposed algorithms are validated by various simulations, and the results suggest promising performance.

Keywords: Urban Air Mobility (UAM), Integrity monitoring, Global Navigation Satellite System (GNSS), Inertial Navigation System (INS), Kalman filter

I. INTRODUCTION

Urban Air Mobility (UAM) refers to a concept proposed to provide short-range, point-to-point air transportation services in metropolitan areas [1]. UAM has recently attracted worldwide interest because of its potential values to the market and the society, such as mitigating ground-based traffic congestion and improving travel efficiency [2]. Safety is the paramount issue for most UAM applications, such as passenger and cargo transportation, for which the airborne navigation system must continuously output accurate and reliable navigation solutions [3, 4]. Therefore, it is imperative to ensure the accuracy and integrity of the navigation system so that it can be competent in UAM applications.

Vertical Takeoff and Landing (VTOL) has been widely acknowledged as an ideal solution for UAM, whose operational phases are generally composed of takeoff, en-route, and landing [5]. This paper only focuses on the en-route phase where the vertiports are beyond the sight of the air vehicles. In this phase, the VTOL vehicles locate themselves through employing Global Navigation Satellite System (GNSS) and other supplementary systems, e.g., Inertial Navigation System (INS). As for the takeoff and landing phases, vision-based or -aided navigation will be the dominant approach because the artificial visual landmarks in the vertiports can make it easy to achieve high navigation accuracy. However, this approach is beyond the scope of this study.

* Manuscript received, June 14, 2020, final revision, October 29, 2020
** To whom correspondence should be addressed, E-mail: xqzhan@sjtu.edu.cn

With more signals and satellites available to the users, GNSS offers better and better navigation performance in terms of accuracy, integrity, continuity and availability. Under open-sky conditions, GNSS currently provides meter-level positioning accuracy by itself and the performance can be further improved by exploiting the differential corrections which greatly mitigate the signal-in-space errors and the atmosphere propagation errors [6]. However, the performance will be severely degraded in urban canyons due to complex signal reflections. In particular, GNSS signals are vulnerable to multipath and None-Line-of-Sight (NLOS) interference, which constitute the major sources of large measurement errors in urban GNSS applications [7].

The navigation system is also confronted with another challenge, i.e., the stringent navigation performance requirements, especially from the integrity perspective. Given that the vehicles will fly over the crowd, failing to correctly perform the navigation task might lead to potentially serious damages to the passengers and people in the vicinity. Therefore, as stated in the definition of integrity, the navigation system should (a) timely notify the user or the control system when it is unavailable and (b) rigorously determine the error bound when it is declared available. The long-term experience in aviation suggests that Aircraft Autonomous Integrity Monitoring (AAIM) is a critical technique to achieve these two objectives [8].

To address the challenges above, we firstly design an integrated navigation system to improve navigation accuracy and robustness. The navigation system is implemented by tightly coupling INS with code-based differential GNSS under an Extended Kalman Filter (EKF) architecture. This system is expected to provide continuous and robust navigation output with high long- and short-term accuracy. It can also enhance navigation integrity because of the additional information redundancy.

Then, integrity monitoring should be embedded in the navigation system so that its integrity can be assured. Although numerous algorithms have been developed to realize integrity monitoring of GNSS-standalone navigation systems, such as Receiver Autonomous Integrity Monitoring (RAIM) [9] and Advanced RAIM (ARAIM) [10], they cannot be directly applied to filter-based integrated navigation systems. This is because the time-sequential error and fault propagation process in the filter makes it difficult to design the fault detection scheme and to derive the upper bound of navigation errors. Our prior work proved that in an EKF architecture, both the current faults and the previous undetected faults can influence the current navigation output [11]. Therefore, it is imperative to design a filter-applicable AAIM framework that can capture all potential faults and rigorously bound the navigation errors coming from measurement noises and undetected faults.

Extensive studies have been carried out to realize fault detection for tightly coupled GNSS/INS [12][13], while they are not AAIM frameworks due to the lack of a rigorous error bound derivation. And in the recent years, there have been some AAIM frameworks developed for GNSS/INS integrated systems, and they can be divided into residual/innovation-based approaches [14][15] and Multiple Hypotheses Solution Separation (MHSS) approaches [16]. It has been proved that the former show a serious disadvantage: as the filter time increases, the integrity risk will gradually rise and eventually become unacceptably high [15, 16]. In contrast, MHSS is free of this problem, and thus it is regarded as a promising solution to the implementation of filter-based AAIM [16].

Therefore, we propose an AAIM framework by employing the MHSS technique in this paper. MHSS is originally utilized in the ARAIM baseline algorithm where multiple subsets are monitored to cope with single and multiple GNSS faults. To leverage this technique in the EKF case, a bank of parallel sub-filters should be maintained aside from the main (i.e., original) filter, each of which is tolerant to a fault mode by rejecting the measurements from one or multiple satellites. MHSS provides two significant benefits as compared to other techniques: it shows promising performance in coping with multiple faults and offers a straightforward proof of integrity [17].

Besides, this paper makes two modifications to the original AAIM framework for accommodating the urban environments. First, we propose an efficient and effective filter bank management strategy to cope with satellite additions and outages. Second, we present a satellite grouping technique which divides the visible satellites into groups to address the two challenges presented in urban environments: multiple faults tend to occur simultaneously, and the faults are likely to be spatially correlated.

The rest of this paper is organized as follows. Section II gives the problem statement and describes the architecture of the integrated navigation system. Then, Section III presents a step-by-step illustration and derivation of the integrity monitoring framework. Next, various simulations are carried out to validate the proposed algorithms in Section IV. Finally, Section V draws the conclusions and discusses prospects for future work.

II. PROBLEM STATEMENT AND NAVIGATION SYSTEM MODELLING

2.1 Problem Statement

To lay the foundation for algorithm design, we clarify the operational conditions in the en-route phase and correspondingly make some assumptions as follows.

The navigation system utilizes the pseudoranges instead of the carrier-phase measurements for the following reasons. First, carriers tend to be unstable in urban environments, which would deteriorate navigation accuracy and integrity [18]. Besides, carrier-based navigation systems necessarily involve the real-time cycle ambiguity determination, which makes it difficult to design the associated integrity monitoring algorithm.

Benefiting from the differential service, the probability of GNSS signal-in-space fault is reduced to a negligible degree. On the other hand, heavy multipath interference and Non-Line-Of-Sight reception become the dominant causes of faults in urban environment. This is because strong signal reflection may occasionally occur due to some tall buildings presenting in the flight path,

which can potentially lead to enormous pseudorange errors.

The air vehicles will not be subject to much signal interference and blockage at one epoch because of their high flight altitudes. Therefore, we assume that the receivers can output adequate fault-free measurements to allow the system to perform integrity monitoring.

2.2 Architecture and Mathematical Model of the Integrated Navigation System

To provide accurate and continuous navigation service, we present an integrated navigation system which employs both GNSS and Inertial Measurement Unit (IMU) measurements. Figure 1 shows the architecture of this system, and the fusion process is illustrated as follows. First, the receiver outputs the pseudoranges which are disrupted by many error components, including signal-in-space errors, atmosphere propagation delays, multipath effects, and receiver noises. Then, the differential corrections significantly reduce the first three terms, leaving multipath and receiver noise as the dominant contributors to pseudorange errors. Finally, differential GNSS and INS are tightly coupled to provide the navigation solutions for the users.

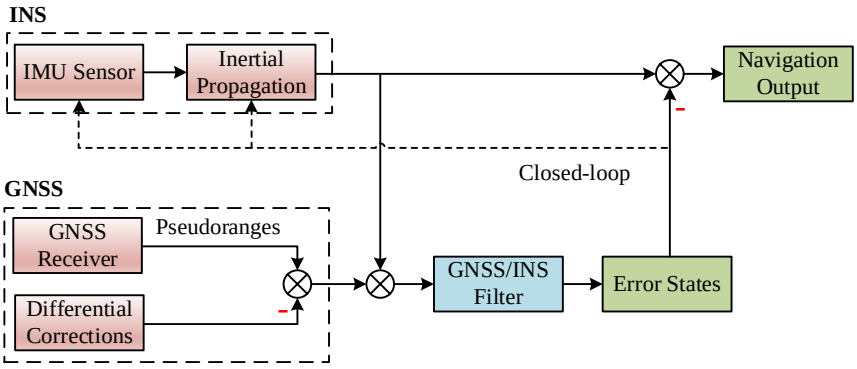

Figure 1 The architecture of the proposed integrated navigation system

As shown in Figure 1, the integration is implemented with a closed-loop error state EKF. In this filter, it is the INS error states rather than the absolute navigation states that are estimated. And at each epoch, the estimated error states are fed back to the INS system, maintaining a linear approximation in the system model. The error state vector is given by the following [19]:

$$x = [\ (\delta\phi)^T,\ \ (\delta v)^T, (\delta p)^T, \nabla_a^T, \nabla_g^T, \delta\rho_u, \delta\dot{\rho}_u]^{\mathrm{T}} \tag{1}$$

where $\delta\phi$ denote the INS attitude errors, δv the INS velocity errors, and δp the INS position errors; ∇_a and ∇_g are the accelerometer and gyro bias vectors; $\delta\rho_u, \delta\dot{\rho}_u$ represent the receiver clock states, i.e., the pseudorange biases caused by clock offset and pseudorange rate bias due to clock drift.

The EKF algorithm is a recursive method using a series of prediction and update steps to obtain the optimal state estimates. As shown in Equations (2) and (3), the prediction step is used to predict the state vector x and its covariance matrix P based on the system process model [19].

$$\hat{x}_k^- = \Phi_{k|k-1}\hat{x}_{k-1}^+ \tag{2}$$

$$P_k^- = \Phi_{k|k-1}P_{k-1}^+\Phi_{k|k-1}^{\mathrm{T}} + Q_k \tag{3}$$

where $\Phi_{k|k-1}$ represents the state transition matrix from epoch $(k-1)$ to epoch k; Q_k is the process noise covariance matrix; the superscripts "-" and "+" respectively denote a predicted (a priori) and an updated (a posteriori) estimates.

When the measurements become available, the filter updates the state vector and the associated covariance matrix by using the measurement model as follows [19]:

$$\hat{x}_k^+ = \hat{x}_k^- + K_k r_k \tag{4}$$

$$P_k^+ = (I - K_k H_k)P_k^- \tag{5}$$

where K_k denotes the Kalman gain matrix, r_k is the innovation vector, and H_k is the measurement matrix.

The innovation vector r_k is defined as the difference between the actual measurement vector z_k and the predicted measurement vector $\hat{z}_k$. The latter is determined based on the measurement matrix and the predicated state vector. Therefore, we have:

$$r_k = z_k - \hat{z}_k = z_k - H_k\hat{x}_k^- \tag{6}$$

When the filter operates in a closed-loop mode, the predicted state vector $\hat{x}_k^-$ is zero because of the feedback process [20].

The gain matrix K_k indicates how much the measurement vector influences the final state estimate. It is obtained by minimizing the variance of the updated state vector and is defined as:

$$K_k = P_k^- H_k^{\mathrm{T}}(H_k P_k^- H_k^{\mathrm{T}} + R_k)^{-1} \tag{7}$$

The equations above briefly describe the mathematical model of tightly coupled GNSS/INS system. More detailed derivations of the process and measurement models can be found in [19].

III. SOLUTION SEPARATION BASED INTEGRITY MONITORING SCHEME

In fault-free cases, the integrated navigation system can continuously output accurate navigation solutions. However, it may encounter abnormally large output errors due to the potential measurement faults. This will lead to a loss of integrity and could place the vehicles in hazardous situations. Therefore, in this section, we develop an integrity monitoring scheme to cope with faulted measurements and to provide safety-assured navigation solutions.

3.1 Bank of Filters Used in MHSS: Generation and Management

Generation of the bank of filters

MHSS is widely utilized by some snapshot GNSS integrity monitoring algorithms, e.g., ARAIM, to realize efficient fault detection and exclusion. Although EKF is a time-sequential estimation method, prior studies have proved its equivalence to the batch Least-Squares estimator that uses all previous measurements [17]. Therefore, MHSS can be introduced to perform integrity monitoring of the tightly coupled GNSS/INS system [16].

To monitor various fault modes, MHSS needs to run a bank of hierarchical filters in parallel, each of which corresponds to a subset of visible satellites. As compared to the main filter which employs all the measurements, single or multiple satellites are excluded in each of the subfilters. The number of filters will be unacceptably large if all the fault modes are monitored. Therefore, as implemented in ARAIM, we can choose to monitor a part of the subsets and use the parameter P_{THRES} to guarantee that the integrity risk coming from unmonitored modes [10] is close to this value. P_{THRES} is an important algorithm parameter because it can not only influence the number of monitored subsets but also the integrity performance. To be more specific, a high P_{THRES} will reduce the number of monitored subsets and increase the total integrity risk.

Handling the addition and outage of satellites

Because the aircraft flies in urban environments, sudden changes may occur to the list of visible satellites due to signal blockage and attitude motion. Special explanations are given to the effect of attitude motion. When the receiver mask angle θ_{min} and the aircraft's attitude are both considered, a visible satellite can be used if the following criteria are simultaneously satisfied: (a) the elevation is larger than θ_{min}; and (b) $\cos(\boldsymbol{l}, \boldsymbol{n}) < (90° - \theta_{min})$, where $\boldsymbol{l}$ is the normalized line-of-sight vector of this satellite, and $\boldsymbol{n}$ is a unit vector that is perpendicular to the antenna plane and points to the sky. Therefore, the attitude motion could lead to the change in the list of visible satellites.

It is worth noting that the monitored filters need to be rearranged when the list of visible satellites changes. Figure 2 presents the strategy of filter bank management to handle the satellite in and out cases. When a new satellite becomes visible, we need to supplement some new filters, including the new main filter and some subfilters, in which the measurements of the new satellite are employed. To avoid the initialization process, these filters are generally branched out from the original ones by inheriting their filter solutions. And when a satellite outage occurs, we can directly remove the filters that have previously used the out-of-view satellite.

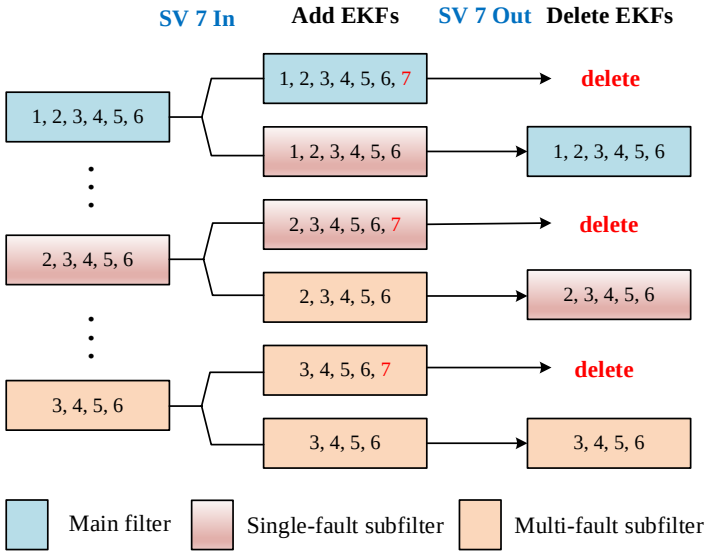

Figure 2 Strategy of filter bank arrangement to handle the addition and outage of satellites

We can prove that this strategy is reasonable by the following statements. First, as proved in the Appendix, the strategy guarantees that in the presence of satellite addition or outage, the integrity risk coming from the unmonitored subsets is only slightly increased or reduced, and therefore it will exert little influence on the integrity performance. Second, in the case of satellite outages, all the remaining filters are only impacted by satellites they use, and they are strictly free of the effect of the suddenly out-of-view satellite. Third, in the case of satellite additions, all the new

filters can inherit the parameters from the original filters so that the initialization process can be avoided.

Satellite grouping

To accommodate the urban GNSS applications, special attention should be paid to the satellite fault probability. In the aviation domain, the failures of two satellites are assumed to be independent, but this is not the case for urban users. In urban environments, the fault events are usually attributed to the heavy signal reflections which are provoked by the surface reflectors (e.g., buildings), and thus there might be a strong spatial dependence between different faults. To explain this in detail, Figure 3 depicts the impacts of surface reflectors on signal receptions by simulating an urban scenario. As shown in this figure, the buildings could simultaneously influence multiple signals from similar directions. Therefore, the occurrence of faults tends to be spatially dependent, and the probability of multiple faults may be much larger than the value obtained under the assumption of fault independence.

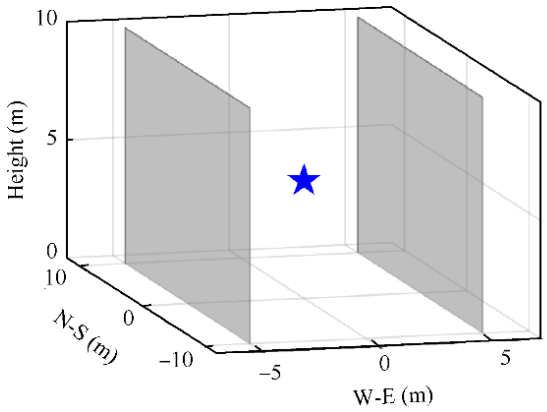

(a) Urban canyon

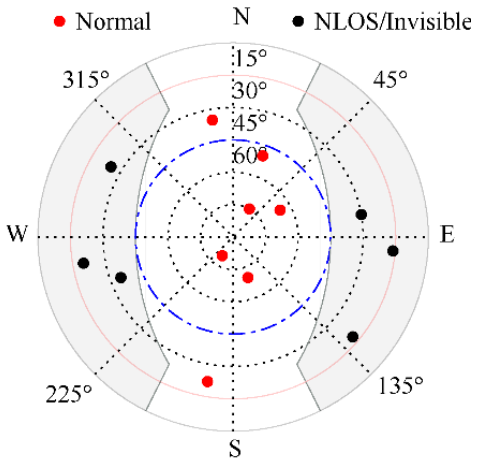

(b) Skyplot

Figure 3 Illustration of signal reception in an urban environment

To address this issue, we propose a satellite grouping approach where utilizing the skyplot, we divide the low-elevation satellites into several non-overlapping groups. In this process, we use the angle between the line-of-sight vectors of two satellites to describe the difference between their signal directions. If this angle is small, the probability that the two satellites are simultaneously faulted will be high. Using this indicator, we present a rationale for the grouping process as follows. First, the low-elevation satellites are picked out using an elevation threshold (e.g., 45°). Then, we manually divide them into non-overlapping non-empty groups, in each of which the maximum angular difference is less than a pre-set threshold (e.g., 45°). This scheme presented here is preliminary, and we will design an automatic and optimal satellite grouping approach in future work.

In the integrity monitoring framework, each satellite group is regarded as an “individual satellite” and is given a group fault probability. Specifically, the original algorithm can be used for the determination of monitored subsets, but it must treat the groups as indivisible individuals. Besides, the handling strategy for the addition or outage of a satellite should be correspondingly modified. Some new filters need to be added if the new satellite forms a new group of its own. And if this satellite joins an existing group, we can simply add it to the filters which use the measurements from the associated group.

3.2 Fault Detection based on Solution Separation

For fault detection, the test statistics are defined by the difference between the mean filter solution and each of the subfilter solution:

$$\Delta y^{(i)} = y^{(i)} - y^{(0)} \tag{8}$$

where y denotes the estimated absolute position vector, the subscript (i) is the index of the subfilter, and the subscript (0) indicates the main filter. Let the index $q = 1$, 2, and 3 designate the east, north, and up components, respectively. For the q th direction, the variances of the subfilter solution and the test statistic are respectively given by [17]:

$$\sigma_q^{(i)2} = \quad C_q^{(i)} \tag{9}$$

$$\sigma_{\mathrm{ss},q}^{(i)2} = \quad C_q^{(i)} - C_q^{(0)} \tag{10}$$

where C represents 3×3 position error covariance matrix extracted from P_k^+, and C_q its qth diagonal component. Then, the detection thresholds for q from 1 to 3 are calculated as:

$$T_1^{(i)} = T_2^{(i)} = Q^{-1}\left({}^{P_{\mathrm{FA\_H}}}\!/_{4N_{\mathrm{S}}}\right) \cdot \sigma_{\mathrm{ss},q}^{(i)2} \tag{11}$$

$$T_3^{(i)} = Q^{-1}\left({}^{P_{\mathrm{FA\_V}}}\!/_{2N_{\mathrm{S}}}\right) \cdot \sigma_{\mathrm{ss},q}^{(i)2} \tag{12}$$

where Q is the tail probability of a zero-mean unit-variance normal distribution and Q^{-1} its inverse; $P_{\mathrm{FA\_H}}$ and $P_{\mathrm{FA\_V}}$ denote the probability of false alert allocated to the horizontal plane and the vertical direction, respectively; and N_{S} is the number of subfilters.

The system can output an assured solution only if for all q and i we have the following:

$$\left|e_q^T \cdot \Delta y^{(i)}\right| \le T_q^{(i)} \tag{13}$$

in which e_q is a 3×1 vector whose qth entry is 1 and all others are 0. If any of the tests fail, the fault detector will issue an alarm to indicate the presence of faults.

3.3 Protection Levels of the Integrated Navigation System

When there is no fault detected, the integrity monitoring scheme needs to determine the Protection Levels (PLs), including Vertical PL (VPL) and Horizontal PL (HPL). The PL is defined as a probabilistic error bound which rigorously captures the impacts of measurement uncertainty and undetected faults [8]. The determination of PLs depends on the integrity requirement, as described by the formula:

$$P_{\mathrm{HMI},q} = \mathrm{Prob}\left\{\left|PE_q\right| < PL_q \ \cap \ \text{no fault alert}\right\} \tag{14}$$

where $P_{\mathrm{HMI},q}$ stands for the integrity budget allocated to the q th direction, PE_q is the position error in this direction, and PL_q the corresponding protection level. Note that, HPL is calculated by $HPL = \sqrt{PL_1^2 + PL_2^2}$, and VPL is equal to PL_3.

MHSS offers a straightforward approach to calculate the PLs by solving the following equation [10]:

$$P_{\mathrm{HMI},q}\left(1 - \frac{P_{\mathrm{NM}}}{P_{\mathrm{HMI}}}\right) = 2Q\left(\frac{PL_q}{\sigma_q^{(0)}}\right) + \sum_i P_{fault}^{(i)} \cdot Q\left(\frac{PL_q - T_q^{(i)}}{\sigma_q^{(i)}}\right) \tag{15}$$

where P_{HMI} denotes the total integrity budget, P_{NM} is the integrity risk coming from unmonitored subsets, and $P_{\mathrm{fault}}^{(i)}$ is the fault probability of subset i.

IV. SIMULATIONS AND RESULTS

This section demonstrates, analyzes, and evaluates the proposed integrity monitoring algorithms for a tightly coupled GNSS/INS system that is designed for UAM applications. For this purpose, we carry out various simulations with some scenarios that are selected to reflect the en-route flight conditions. Using these simulations, we evaluate the achievable integrity performance and analyze its sensitivity to various factors.

4.1 Simulation Set-up

First, we establish a software-defined simulator of the GNSS/INS integrated navigation system. This simulator generates a flight trajectory and simulates both GNSS and IMU measurements following the state-of-the-art error models [20]. To conduct sensitivity analyses, we select two different grades of IMU sensors and consider the availability of differential GNSS service. The simulation parameters and the error settings are summarized in Table 1. Note that, the high-grade IMU has similar performance with the module ADIS16500, and the low-grade one is similar to ADIS16362 [21].

The simulated flight trajectory is depicted in Figure 4, which consists of leveling, turning, and descending phases. The receiver mask angle is set to 15 degrees, and Figure 5 presents the skyplot of the visible satellites during the simulation.

Table 1 The simulation parameters and error models

Sensor	Parameters	Values (high-grade)	Values (low-grade)
IMU	Angular random walk	0.2 °/$\sqrt{\text{hr}}$	2 °/$\sqrt{\text{hr}}$
	Velocity random walk	20 μg/$\sqrt{\text{Hz}}$	100 μg/$\sqrt{\text{Hz}}$
	In-run gyroscope bias noise	8 °/hr ; τ = 3000 s	25 °/hr ; τ=3000s
	In-run accelerator bias noise	15 μg ; τ = 10000 s	100 μg ; τ=10000s
	Sampling rate	100 Hz	100 Hz
Sensor	Parameters	Values (differential)	Values (undifferential)
GNSS	Multipath and receiver noise	0.8 meter [22]	0.8 meter
	Other noise terms	0.1 meter	2 meters
	Constellation	GPS	GPS
	Sampling rate	1 Hz	1 Hz

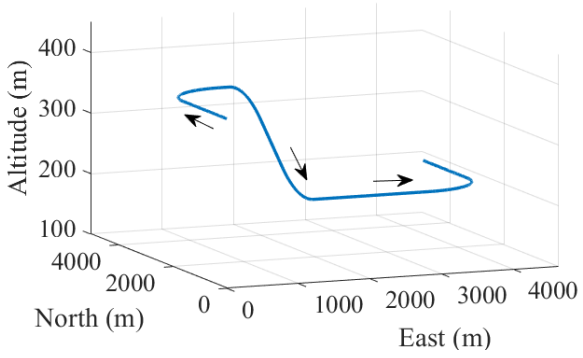

Figure 4 The simulated flight trajectory where the start point locates at (30°N, 120°E)

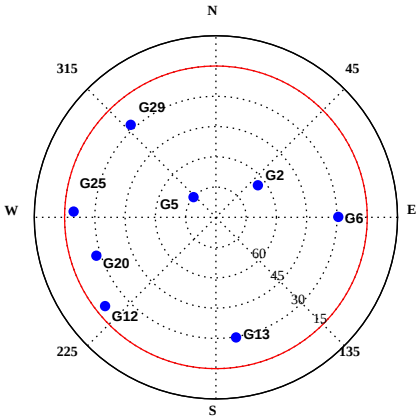

Figure 5 The skyplot of the visible satellite

4.2 Validation of the proposed algorithms

In this section, we intend to examine the effectiveness of the proposed integrity monitoring scheme. The following simulations are based on a baseline sensor configuration where the differential service is available and the high-grade IMU is used. Table 2 gives the input parameters of the integrity monitoring algorithm. These values stem from the aviation domain and they can

represent the typical integrity and continuity requirements in safety-critical applications. To carry out a detailed analysis, we simulate various fault scenarios by manually adding different faults to the raw GNSS pseudoranges. Without loss of generality, we only focus on the trajectory of the first 100s. And in each scenario, the faults are injected during 30s to 100s.

Table 2 The list of input parameters [10]

Name	Description	Values
$P_{\mathrm{HMI},1}$	Integrity budget allocated to east direction	9.8×10^{-8}
$P_{\mathrm{HMI},2}$	Integrity budget allocated to north direction	1×10^{-9}
$P_{\mathrm{HMI},3}$	Integrity budget allocated to up direction	1×10^{-9}
$P_{\mathrm{FA\_H}}$	False alert probability in the horizontal plane	9×10^{-8}
$P_{\mathrm{FA\_V}}$	False alert probability in the vertical direction	3.9×10^{-6}
P_{THRES}	Threshold for the integrity risk from unmonitored subsets.	8×10^{-8}

First, we simulate three single-fault cases where the step faults of 3m, 5m, and 10m are respectively injected into the pseudoranges of G25. The probability of individual satellite fault is set to 10^{-5}. Figure 6 presents the test statistics and the thresholds in these scenarios. And Figure 7 shows the associated position errors and protection levels. On the one hand, it is apparent from Figure 6 that the larger the fault magnitude is, the easier and faster the detection will be. On the other hand, Figure 7 suggests that there is clearly a positive correlation between the fault magnitude and the position error. Furthermore, this figure indicates that when there is no fault alarm, the protection levels can strictly bound the corresponding position errors. In summary, the figures reflect the two objectives of the integrity monitoring scheme: one is to detect the measurement faults, and the other is to provide an error bound which captures the impacts of undetected faults.

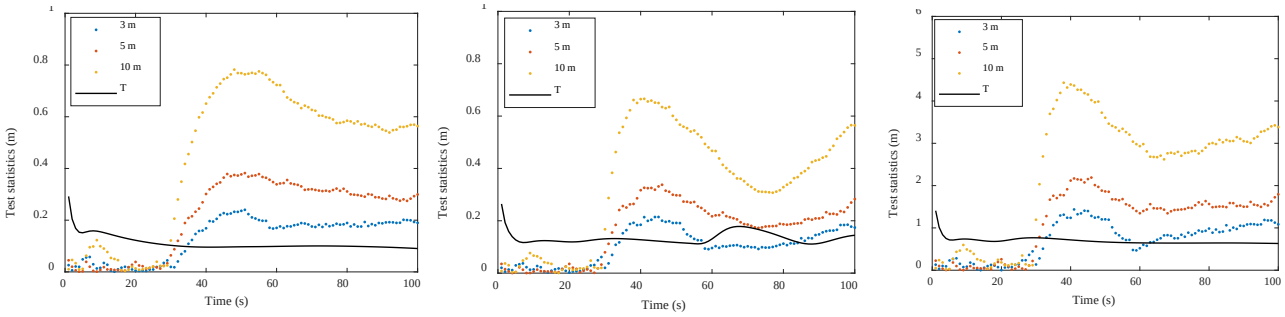

(a) Up (b) North (c) East

Figure 6 Test statistics and thresholds (T) under various single step fault conditions

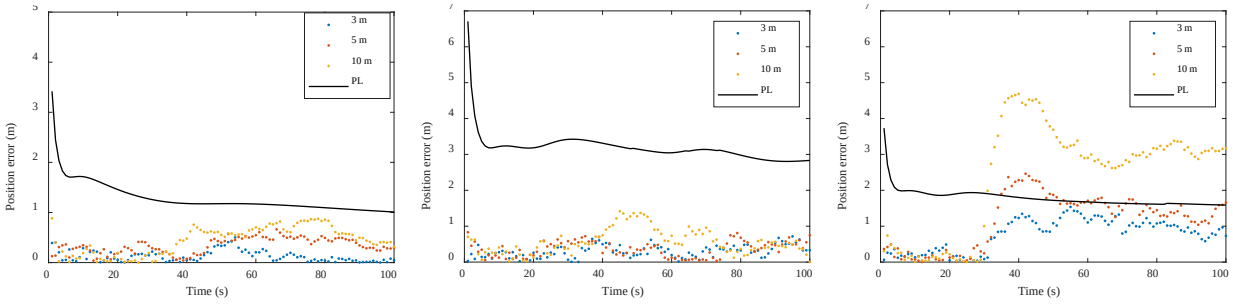

(a) Up (b) North (c) East

Figure 7 Position errors and protection levels under various single step fault conditions

Then we replace the step faults with slowly growing errors to further demonstrate the algorithm performance. Figure 8 gives the test statistics and the thresholds under different fault slopes, including 0.1m/s, 0.2m/s and 0.5m/s. And Figure 9 shows the corresponding position errors and protection levels. It can be seen from the figures that, for one thing, there is an obvious detection delay in these cases, especially for the faults with small slopes. For another, the protection level can generally provide a safe error bound before the associated detection point.

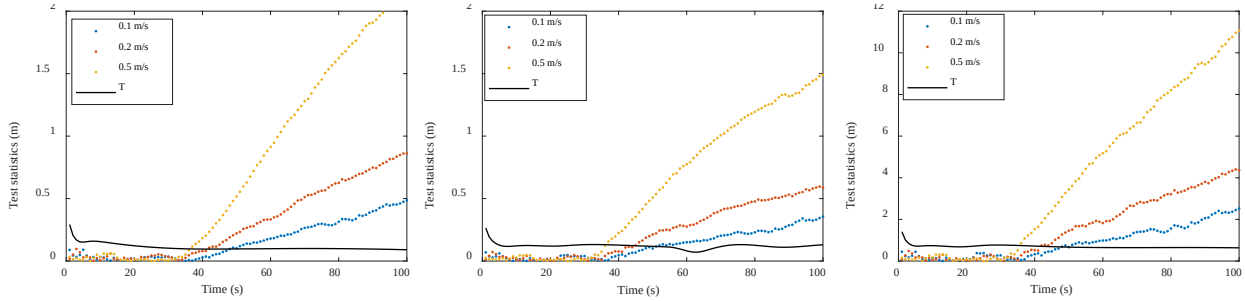

(a) Up (b) North (c) East

Figure 8 Test statistics and thresholds (T) under various single ramp fault conditions

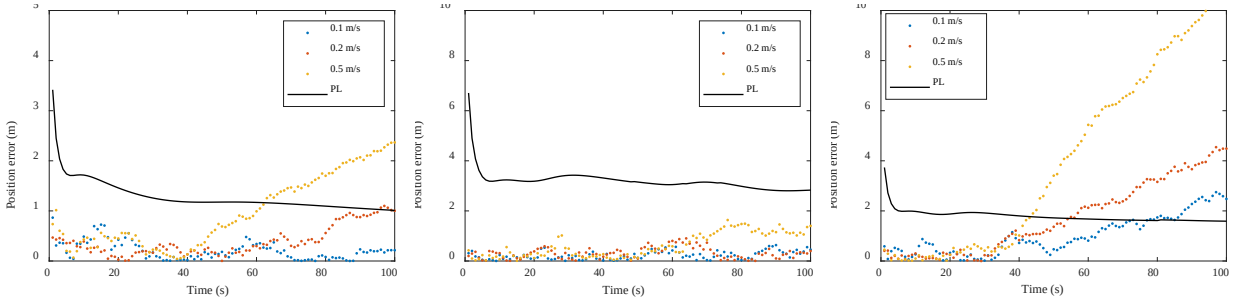

(a) Up (b) North (c) East

Figure 9 Position errors and protection levels under various single ramp fault conditions

In addition, the integrity monitoring scheme needs to provide promising performance in the presence of multiple simultaneous faults. To validate this, we inject two 5-meters step faults to the pseudoranges of G12 and G25, respectively. The prior probability of satellite fault is set to 10^{-4} in this case. According to the test results shown in Figure 10, the proposed scheme can also protect the navigation system against multiple faults. Additionally, it is worth mentioning that the fault detection algorithm cannot cope with the fault modes that are not monitored by MHSS. In other words, the detection result is no longer reliable in these cases. In the meanwhile, these modes are unlikely to happen, and the total probability of their occurrence will not exceed the preset threshold P_{THRES}.

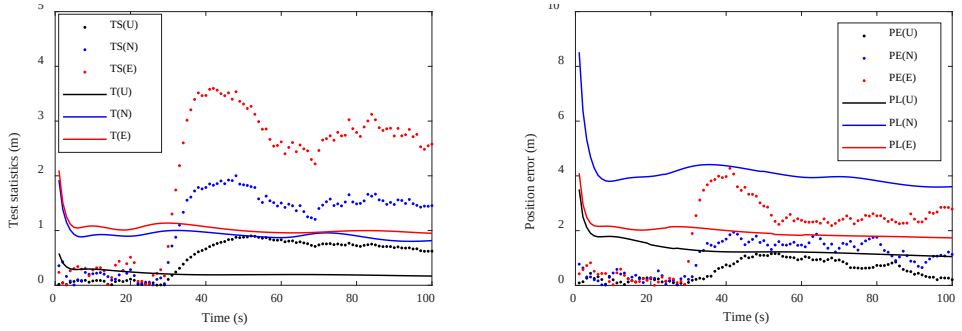

(a) Test statistics and thresholds (b) Position errors and protection levels

Figure 10 The test results under multi-fault conditions

In urban environments, the occurrence of different satellite faults may be spatially dependent. And in Section 3.1, we propose a satellite grouping technique to address this issue. The following simulation intends to analyze the algorithm behaviors after performing satellite grouping. According to the skyplot above, G12, G20, and G25 will form a satellite group (labeled as Group 1), and each of the rest satellites will form a separate group. The prior probability of group fault is set to 10^{-5}. Then we add 5-meters step faults to the measurements of every satellite in Group 1, and Figure 11 displays the corresponding results in this scenario. It is obvious that the integrity monitoring scheme is also effective and efficient in the presence of group faults.

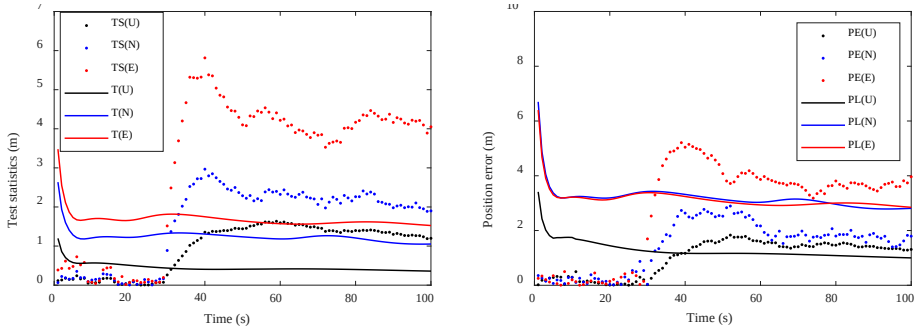

(a) Test statistics and thresholds (b) Position errors and protection levels

Figure 11 The test results in the presence of a group fault

4.3 Sensitivity Analyses

In this section, we carry out a sensitivity analysis to quantify the impacts of various factors on navigation performance. Based on the sensor parameters shown in Table 1, we first analyze the impacts of pseudorange accuracy and IMU performance. The satellite fault probability is set to 10^{-5}, and the values of input parameters are shown in Table 2. Figure 12 presents the protection levels under different sensor configurations. The results suggest that integrity performance can be significantly improved by subscribing GNSS differential services and employing high-grade IMU sensors. In this simulation, the parameters of the high-grade IMU represent a typical high-precision miniature sensor whose price is approximately $300 [21]. Therefore, this sensor is economically viable for UAM applications. Besides, with the continuous development of land-based augmentation systems, the users will have easy access to the GNSS differential service soon. Additionally, it is expected that the navigation performance can be further enhanced by employing the measurements from multiple constellations, which will be investigated in future work.

Also, the prior fault probability could impact the protection levels. To conduct quantitative analysis, we select the three settings of this parameter as follows: (a) 10^{-5} for each satellite, (b) 10^{-4} for each satellite, or (c) 10^{-5} for each satellite group. Figure 13 compares the protection levels under these conditions. As shown in this figure, setting a higher fault probability and applying the satellite grouping approach can both lead to the increases in the protection levels. Besides, we can see that there is a considerable variation in the increased value among different directions. This phenomenon is mainly attributed to satellite geometry (see Figure 5). Specifically, fault probabilities determine the monitored fault modes, and the contribution of each fault mode to the integrity risk heavily depends on the satellite geometry. For the same reason, a fault mode can generally exert different impacts on the protection levels of different directions.

Finally, we analyze the impacts of satellite addition and outage on the protection levels. Figure 14 compares the time-varying protection levels among three cases: the baseline, satellite addition, and satellite outage. In the baseline case, all the visible satellites are used in the main filter. And G25 is assumed invisible before 50s to simulate a satellite addition case. Similarly, this satellite is assumed out of view at 50s for the simulation of a satellite outage. The addition and outage of a satellite can be caused by the attitude motion of the aircraft or the signal blockage. The results imply that a new satellite becoming visible can result in the decreases in the protection levels while a satellite outage can lead to the increases. Besides, it is observed that only the east protection level is significantly influenced. The underlying cause of this phenomenon is that the addition and outage of G25 mainly impact the satellite geometry in the east-west direction. Moreover, this simulation also proves the effectiveness of the proposed scheme in handling satellite changes.

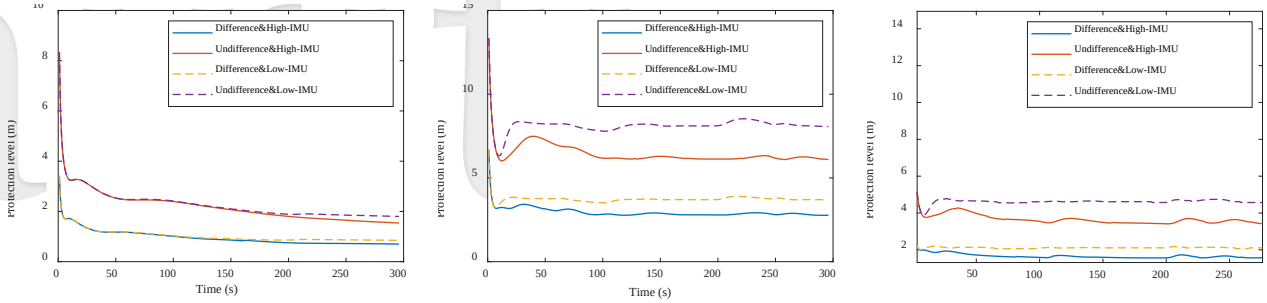

(a) Up (b) North (c) East

Figure 12 Protection levels under various sensor configurations

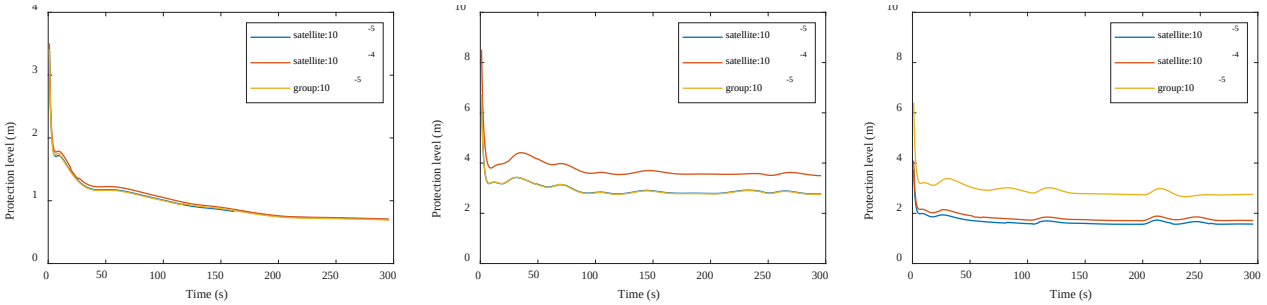

(a) Up (b) North (c) East

Figure 13 Protection levels under various settings of fault probabilities

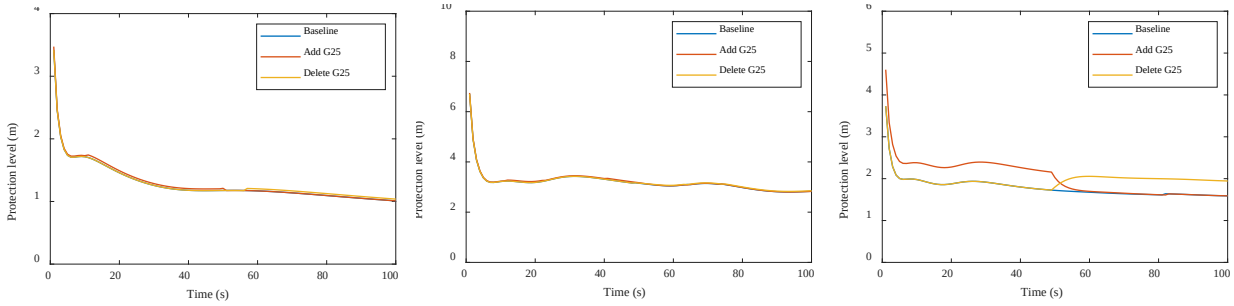

(a) Up (b) North (c) East

Figure 14 The impacts of satellite addition and outage on protection levels

V. CONCLUSIONS

This paper develops, analyzes, and validates a multi-sensor integrated navigation system to support the en-route flight in UAM applications. This system combines differential GNSS and INS in an EKF-based tight coupling framework and is embedded with an integrity monitoring scheme to ensure navigation integrity. Besides, we propose a fault grouping technique to accommodate the spatial correlation between different satellite faults. Simulations are carried out to validate the algorithms, and the results suggest the high efficiency and effectiveness of the scheme in coping with various types of measurement faults. In addition, the sensitivity analyses demonstrate that both the IMU grade and the pseudorange accuracy can significantly impact the navigation performance.

Future work will focus on the following aspects: (a) extending the scheme to multi-constellation GNSS; (b) validating the algorithms by real-world flight experiment; and (c) reducing the algorithm complexity.

ACKNOWLEDGMENTS

This work is supported by Shanghai Jiao Tong University (SJTU) Global Strategic Partnership Fund (2019 SJTU – UoT) and the Research Achievements Industrialization Foundation of the MoE Research Center on Aerospace Science and Technology.

APPENDIX

This appendix analyzes the effect of satellite addition and outage on the integrity risk P_{NM} coming from the unmonitored subsets.

When a new satellite becomes visible, the unmonitored subsets at this epoch are composed of two groups: (a) the group of original unmonitored subsets, $\mathcal{G}_o$, and (b) the group of new unmonitored susbets, $\mathcal{G}_n$. Each subset in $\mathcal{G}_n$ is obtained by adding the new satellite to the corresponding subset in $\mathcal{G}_o$. Therefore, the new P_{NM} is determined by the following:

$$P_{\mathrm{NM,new}} = P_{\mathrm{NM,old}} + P_{\mathrm{NM,old}} \times P_{\mathrm{sat,add}} \tag{A1}$$

where $P_{\mathrm{NM,old}}$ is the original P_{NM}, and $P_{\mathrm{sat,add}}$ is the prior fault probability of the new satellite. The satellite fault probability is usually lower than 10^{-2}, and thus the P_{NM} is only slightly increased in the addition of a satellite. And when multiple satellites simultaneously become invisible, the new P_{NM} can also be calculated using Equation (A.1), by regarding that the satellites are added to the list of visible satellites one by one.

In the case of a satellite outage, we can determine the new P_{NM} as follows:

$$P_{\mathrm{NM,new}} = P_{\mathrm{NM,old}} - P_{\mathrm{NM,old}} \times P_{\mathrm{sat,out}} \tag{A2}$$

where $P_{\mathrm{sat,out}}$ is the prior fault probability of the out-of-view satellite. The derivation is similar to that shown above, and thus it is omitted for brevity.

REFERENCES

[1] Vascik PD, Hansman RJ, Dunn NS, "Analysis of Urban Air Mobility Operational Constraints," *Journal of Air Transportation*, Vol. 26, No. 4, 2018, pp. 133–146.

[2] Booz Allen Hamilton, "Urban Air Mobility (UAM) Market Study," 2018. Presented to NASA-Aeronautics Research Mission Directorate. Oct. 5, 2018. Available at: https://www.nasa.gov/uamgc

[3] NASA Glenn Research Center, "Federal Contract Opportunity for Reliable, Secure, and Affordable CNS Options for Urban Air Mobility," April 19, 2019. Available at: https://govtribe.com/opportunity/federal-contract-opportunity/

[4] Thipphavong DP et al., "Urban air mobility airspace integration concepts and considerations," 2018 Aviation Technology, Integration, and Operation Conference, 2018.

[5] Silva C, Johnson W, Antcliff KR, Patterson MD, "VTOL urban air mobility concept vehicles for technology development," 2018 Aviation Technology, Integration, and Operation Conference, 2018, pp.1–16.

[6] Marila S, Bhuiyan MZH, Kuokkanen J, Koivula H, Kuusniemi H, "Performance comparison of differential GNSS, EGNOS and SDCM in different user scenarios in Finland," 2016 Europe Navigation Conference (ENC) 2016, 2016.

[7] Smolyakov I, Rezaee M, Langley RB, "Resilient multipath prediction and detection architecture for low-cost navigation in challenging urban areas," Proceedings of 32nd International Technical Meeting Satellite Division Institute of Navigation (ION GNSS+ 2019), 2019, pp. 175–188.

[8] Zhu N, Marais J, Betaille D, Berbineau M, "GNSS Position Integrity in Urban Environments: A Review of Literature," *IEEE Transactions on Intelligent Transportation System*, Vol. 19, No. 9, 2018, pp. 2762–2778.

[9] Hewitson S, Wang J, "GNSS receiver autonomous integrity monitoring (RAIM) performance analysis," *GPS Solutions*, Vol. 10, No. 3, 2006, pp. 155–170.

[10] Blanch J, et al., "Baseline advanced RAIM user algorithm and possible improvements," *IEEE Transactions on Aerospace and Electronic System*, Vol. 51, No. 1, 2015, pp. 713–732.

[11] Wang SZ, Zhan XQ, Zhai YW, Liu BY, "Fault detection and exclusion for tightly coupled GNSS/INS system considering fault in state prediction," *Sensors (Switzerland)*, Vol. 20, No. 3, 2020.

[12] Wang SZ, Zhan XQ, Pan WC, "GNSS/INS tightly coupling system integrity monitoring by robust estimation," *Journal of Aeronautics, Astronautics, and Aviation*, Vol. 50, No. 1, 2018, pp. 61–80.

[13] Yang L, Li Y, Wu YL, Rizos C, "An enhanced MEMS-INS/GNSS integrated system with fault detection and exclusion capability for land vehicle navigation in urban areas," *GPS Solutions*, Vol. 18, No. 4, 2014, pp. 593–603.

[14] Joerger M, Pervan B, "Kalman Filter-Based Integrity Monitoring Against Sensor Faults," *Journal of Guidance, Control, and Dynamics*, Vol. 36, No. 2, 2013, pp. 349–361.

[15] Tanıl Ç, Khanafseh S, Joerger M, Pervan B, "Sequential integrity monitoring for Kalman filter innovations-based detectors," Proceedings of the 31st International Technical Meeting of the Satellite Division of The Institute of Navigation (ION GNSS+ 2018), 2018, pp. 2440-2455.

[16] Tanıl Ç, et al., "Optimal INS/GNSS coupling for autonomous car positioning integrity," Proceedings of the 32nd International Technical Meeting of the Satellite Division of The Institute of Navigation (ION GNSS+ 2019), 2019, pp. 3123–3140.

[17] Gunning K, Blanch J, Walter T, Groot L, Norman L, "Design and evaluation of integrity algorithms for PPP in kinematic applications," Proceedings of 31st

International Technical Meeting Satellite Division Institute of Navigation (ION GNSS+ 2018), 2018, pp. 1910–1939.

[18] Humphreys TE, Murrian M, Narula L, "Low-cost precise vehicular positioning in urban environments," Proceedings of 2018 IEEE/ION Position, Location, Navigation Symposium, 2018, pp. 456–471.

[19] Angrisano A, "GNSS/INS Integration Methods," Ph.D. Dissertation. University of Calgary, 2010.

[20] Groves PD, Principles of GNSS, Inertial and Multi-Sensor Integrated Navigation Systems. 2nd Edition. London: Artech House, 2013.

[21] Analog Devices, "Inertial Measurement Units (IMU) Datasheet." [Online]. Available at: https://www.analog.com/en/parametricsearch/11172#/.

[22] Salós D, Macabiau C, Martineau A, Bonhoure B, Kubrak D, "Nominal GNSS pseudorange measurement model for vehicular urban applications," Proceedings of 2010 IEEE/ION Position, Location, Navigation Symposium, 2010, pp. 806–815.